

Interplay between heavy fermions and crystal-field excitation in Kondo lattices: Low-temperature thermodynamics and inelastic neutron scattering spectra of CeNiSn

Yu. Kagan, K. A. Kikoin, and A. S. Mishchenko

Kurchatov Institute, Moscow 123182, Russia

(Received 23 October 1996)

The microscopic theory of interaction between the heavy fermions and the crystal-field excitations in Kondo lattices is presented. It is shown that the heavy-fermion spectrum scaled by the Kondo temperature T_K can be modified by the crystal-field excitations with the energy Δ_{CF} provided the inequality $\Delta_{CF} < T_K$ is realized. On the base of the general description of the excitation spectrum, the detailed qualitative and quantitative explanation of anisotropic inelastic neutron scattering spectra and low-temperature specific heat of orthorhombic CeNiSn is given. The theory resolves the apparent contradiction between the metallic conductivity and the gapwise behavior of thermodynamic properties and spin response of CeNiSn at low temperatures. [S0163-1829(97)01514-2]

I. INTRODUCTION

Although the heavy-fermion (HF) behavior of the rare-earth- and actinide-based intermetallics is related to the localized electrons in the $4f$ and $5f$ shells of Ce and U, the influence of the crystal-field (CF) splitting of the f levels is inessential, as a rule, for the low-energy excitations in these systems, since the inequality $\Delta_{CF} \gg T^*$ is valid for most of these compounds.¹ Here $T^* \sim T_K$ is the temperature which characterizes the energy scale of the HF spectrum. The only role of this interaction is to form the ground state Kramers doublet which is the eventual source of the low-energy excitations with extremely high density of states. However, the picture changes radically when this inequality is violated. One can expect that in the case of $\Delta_{CF} < T^*$ the inevitable interplay between the local CF excitations and itinerant HF's should result in appearance of the fine structure in the low-energy spectrum which should be characterized by at least two additional energy parameters, i.e., the position of the CF level and the magnitude of intermixing. This interplay should result in remarkable changes in the spectral and thermodynamic properties of the system in the temperature interval $0 < T < \Delta_{CF}$, although it is clear that the characteristic HF behavior of the system should persist at $T \rightarrow 0$: the Fermi-liquid-like temperature dependences for the specific heat, $C(T) \sim T$, electrical resistivity, $\rho(T) - \rho(0) \sim T^2$, NMR relaxation rate, $T_1 T = \text{const}$, etc., should be observed, although the coefficients in these laws should be sensitive not only to T^* but also to these new parameters. On the other hand, the hybridization of the HF and CF excitation can result, as it frequently occurs, in appearance of the pseudogap in the energy spectrum, although this pseudogap should be characterized mainly by the crystal field and mixing parameters.

The idea of applying these considerations to a description of unusual properties of CeNiSn was proposed in Ref. 2. It was shown that one of the necessary preconditions for realization of this mechanism is the specific picture of CF level splitting: it was supposed that the two lowest Kramers dou-

plets of the $Ce(f^1)$ configuration are separated by a small energy gap:

$$\Delta_{CF} < T^*, \quad (1)$$

while the distance between the ground state and the second excited level is much larger, $\Delta'_{CF} \gg \Delta_{CF}$. The characteristic HF energy T^* is estimated as 40–80 K from various experimental data for CeNiSn.³ Later on, the indirect measurements by Alekseev *et al.*⁴ confirmed assumption (1). In that paper the crystal field was measured on the Nd ion in $Nd_{0.3}La_{0.7}Ni$ crystal which is equivalent to CeNiSn from the point of view of the rare-earth (RE) crystalline environment and lattice spacings. The crystal field acting at the RE site was restored from measured CF splitting of the Nd f level and then recalculated for the case of the Ce ion with the same parameters of an equivalent CF Hamiltonian in an approximation of a purely electrostatic field. The CF splitting energies were estimated as $\Delta_{CF} \approx 4.4$ meV and $\Delta'_{CF} \approx 14.0$ meV, which is consistent with the assumption of Ref. 2 and inequality (1).

Another experimental result crucial for the above general consideration was the observation of Fermi-liquid behavior at a low enough temperature in good quality samples of CeNiSn and CeRhSb. It was found that these samples demonstrate the metallic T^2 dependence of electrical resistivity at $T < 7$ K,⁵ the NMR relaxation rate returns to Korringa law at $T < 1$ K,⁶ and the limiting value of the Sommerfeld coefficient γ in the linear- T term of $C(T)$ is $\gamma = 40$ mJ/K² mol at 0.03 K.⁵ This value is noticeably lower than that predicted by the high-temperature estimations of T^* . These results seemed to be striking, since the semiconductorlike rise of the resistivity and T^3 dependence of $1/T_1$ was observed earlier on the less perfect samples.³

The most challenging experimental observations on CeNiSn are the inelastic magnetic neutron scattering spectra which demonstrate extremely complicated (\mathbf{Q}, ω) -dependent structures with quasigap behavior for some directions of \mathbf{Q} .⁷⁻¹⁰ All these features disappear completely at $T = 25$ K. This picture is inexplicable in terms of

standard notions of intersite spin fluctuations. At the same time, these data are highly informative from the point of view of the structure of low-energy spin excitations, so the adequate interpretation of the neutron scattering data is the most effective criterion for selecting out various theoretical interpretations.

In the present paper the spectral properties of CeNiSn are analyzed on the base of the ideas formulated in Ref. 2 and applied for the quantitative explanation of low-temperature thermodynamics in Refs. 2 and 11. We apply these ideas to the spin liquid which is formed in Kondo lattices, provided the magnetic order does not appear at low temperature. We describe this spin liquid in terms of resonating valence bond (RVB) excitations similar to those introduced by Anderson and used later in a description of the nearly magnetic state in two-dimensional (2D) Cu-O planes of high- T_c materials.¹² In this case the characteristic properties of the HF liquid are determined by the subsystem of spin excitations (spinons) which obey Fermi statistics at low temperature. The stabilization mechanism for the RVB state in 3D Kondo lattices was offered in Ref. 14. We modify the theory of a spin liquid for the case of $\Delta_{\text{CF}} < T_K$, calculate the spectrum of RVB excitations for a special case of an orthorhombic CeNiSn lattice, and give a detailed comparison of a calculated neutron scattering cross section with the experimental results of Refs. 9 and 10. The quasi-2D character of spin excitations discovered in these experiments is essentially used in our calculations. Quite reasonable agreement between the theoretical curves and experimental constant- \mathbf{Q} and constant- E scans seems encouraging. To make an additional test of adequacy of the theory, we also calculate the low-temperature specific heat of CeNiSn within the same set of model parameters.

II. DEGENERATE SPIN LIQUID IN A CRYSTAL FIELD

The theory of the HF systems starts with the Anderson lattice Hamiltonian. In a special case of $\text{Ce}^{(3+)}(f^1)$ ions in a crystal field this Hamiltonian is usually written as

$$H = H_f + H_c + H_{cf} + H'. \quad (2)$$

Here H_f describes the Ce ions in a crystal field,

$$H_f = \sum_{\mathbf{i}, \Lambda} E_{\Gamma} f_{\mathbf{i}\Lambda}^{\dagger} f_{\mathbf{i}\Lambda} + \frac{U}{2} \sum_{\mathbf{i}, \Lambda \neq \Lambda'} f_{\mathbf{i}\Lambda}^{\dagger} f_{\mathbf{i}\Lambda} f_{\mathbf{i}\Lambda'}^{\dagger} f_{\mathbf{i}\Lambda'}, \quad (3)$$

$f_{\mathbf{i}\Lambda}^{\dagger}$ is the creation operator of the f electron in a state $\Lambda = \Gamma \nu$ in a site \mathbf{i} , where ν is the row of the irreducible representation Γ of the crystal point group, E_{Γ} denotes the energy of the f level in the electrostatic crystal field, and U stands for the Coulomb repulsion between the f electrons in the same site. The f ions are immersed in a Fermi sea of conduction electrons which are described by the Hamiltonian

$$H_c = \sum_{k, \Lambda} \epsilon_{k\Gamma} c_{k\Lambda}^{\dagger} c_{k\Lambda}. \quad (4)$$

The third term in the Hamiltonian (2) describes the hybridization between f and conduction electrons,

$$H_{cf} = \sum_{kk'} \sum_{\mathbf{i}} \sum_{\Lambda} (V_{k\Lambda}^{\dagger} f_{\mathbf{i}\Lambda}^{\dagger} c_{k\Lambda} + \text{H.c.}). \quad (5)$$

The so-called Coqblin-Cornut (CC) approximation^{15,16} which represents the Bloch functions by their partial waves $c_{k\Lambda}^{\dagger}$, and takes into account only the diagonal in Λ hybridization matrix elements $V_{k\Lambda}^{\dagger} = \langle \mathbf{k}\Lambda | V | \mathbf{i}\Lambda \rangle$ is used. All the one-electron processes beyond this approximation are collected in the last term H' in the Hamiltonian (2).

It is widely believed that the $s = 1/2$ approximation for the total moment j of $\text{Ce}(f^1)$ ion works well in the Anderson lattice Hamiltonian because the CF splitting of the sextet $j = 5/2$ usually results in a simple Kramers doublet ground state, and the CF splitting exceeds essentially the characteristic interaction energy T_K . This procedure seems to be reasonable when one deals with the ground state and the low-energy excitations with characteristic frequencies $\hbar\omega < \Delta_{\text{CF}}$. Since our task is inclusion of CF excitations in the general picture of spin liquid behavior, we should begin with generalization of $s = 1/2$ theory for the case of a realistic crystal-field scheme.

The Kondo lattice deals with the well-localized f electrons for which the inequality $V_{k\Lambda} \ll \epsilon_F - E_f$, where E_f is the energy level of a free $\text{Ce}(f^1)$ ion, is assumed to be valid, and the Hubbard parameter U is taken large enough to suppress the doubly occupied f states of this ion. In this case the canonical transformation eliminating the hybridization interaction from the Hamiltonian (2) can be done (see Ref. 16), and the effective Hamiltonian projected to the subspace of homopolar states with $n_f = 1$ can be written as

$$H^{(\text{CC})} = H_f + H_c + H_{\text{ex}} + H_h, \quad (6)$$

where

$$H_{\text{ex}} = \sum_{kk'} \sum_{\mathbf{i}} \sum_{\Lambda, \Lambda'} J_{\mathbf{i}}^{\Lambda\Lambda'}(k, k') f_{\mathbf{i}\Lambda}^{\dagger} f_{\mathbf{i}\Lambda'} c_{k'\Lambda'}^{\dagger} c_{k\Lambda} \quad (7)$$

describes the effective sf -exchange interaction, and

$$H_h = - \sum_{k > k_F} \sum_{\mathbf{i}} \sum_{\Lambda} J_{\mathbf{i}}^{\Lambda\Lambda}(k, k) f_{\mathbf{i}\Lambda}^{\dagger} f_{\mathbf{i}\Lambda} \quad (8)$$

corresponds to effective covalent contribution to the one-site CF splitting due to virtual sf transitions. Here

$$J_{\mathbf{i}}^{\Lambda\Lambda'}(k, k') = \frac{V_{k\Lambda}^{i*} V_{k'\Lambda'}}{\epsilon_k - E_f}. \quad (9)$$

We assume for the sake of simplicity that the conduction electrons are degenerate in Λ near the electron Fermi surface and neglect the CF splitting of the f level in the denominator of the effective sf -exchange integral.

We are interested in the case of $n_f = 1$ when the charge fluctuations in the f channel are completely suppressed. Then, according to the scenario of Refs. 14 and 17, the neutral spin liquid should arise at some temperature $T^* \sim T_K$ instead of antiferromagnetic or Kondo-singlet state offered by the standard Doniach dichotomy. And, as a result, the spin liquid excitations together with the low-energy electrons turn out to be responsible for the low-temperature thermodynamics of the Kondo lattice. Now we incorporate the CF

excitations in this picture. The ‘‘fast’’ electrons with characteristic energies $\hbar\omega > T_K$ are responsible for formation of the spin-spin correlation at $T > T_K$ [the Kondo temperature is defined as $T_K \approx \epsilon_f \exp(-1/2\alpha)$, where $\alpha = J_{sf} \mathcal{N}(\epsilon_F)$, $J_{sf} = |V_{k_F}|^2 / (\epsilon_F - E_f)$, and $\mathcal{N}(\epsilon_F)$ is the electron density of states at Fermi level]. These fast electrons can be integrated out, and the effective Hamiltonian for the spin degrees of freedom can be written in the following form:

$$H^s = H_f + H'_h + H_{\text{RKKY}}^{(g)} + H_{\text{RKKY}}^{(nd)}, \quad (10)$$

$$H_{\text{RKKY}}^{(g)} = \sum_{\mathbf{i}\mathbf{i}'}^{\mathbf{i}\neq\mathbf{i}' } \sum_{\nu\nu'} I_{\mathbf{i}\mathbf{i}'}^{GG} f_{iG\nu}^\dagger f_{iG\nu'} f_{i'G\nu'}^\dagger f_{i'G\nu}, \quad (11)$$

$$H_{\text{RKKY}}^{(nd)} = \sum_{\mathbf{i}\mathbf{i}'}^{\mathbf{i}\neq\mathbf{i}' } \sum_{E\nu\nu'} I_{\mathbf{i}\mathbf{i}'}^{GE} f_{iG\nu}^\dagger f_{iE\nu'} f_{i'E\nu'}^\dagger f_{i'G\nu}. \quad (12)$$

Here the notations $\Lambda = G\nu$ and $\Lambda = E\nu$ are used for the ground state and excited states, respectively, H'_h includes the scattering correction to the CF level renormalization due to the interaction H_{ex} ,

$$I_{\mathbf{i}\mathbf{i}'}^{GG} \sim \alpha^2 \Phi_G(\mathbf{k}_F, \mathbf{R}_i - \mathbf{R}_{i'}) B_G(\theta, \phi) K(T) \quad (13)$$

is the indirect exchange interaction which contains an oscillating RKKY function $\Phi_G(\mathbf{k}_F, \mathbf{R}_i - \mathbf{R}_{i'})$, anisotropy factor $B_G(\theta, \phi)$ (θ is the angle between the z axis which is assumed to be the axis of magnetic quantization, and the line connecting the ions \mathbf{R}_i and $\mathbf{R}_{i'}$, and ϕ is the angle of rotation about the z axis (see the Appendix), and an additional enhancement factor $K(T)$ due to the high-temperature one-site Kondo scattering.¹⁴ $I_{\mathbf{i}\mathbf{i}'}^{GE}$ is the integral of the same type as that in Eq. (13), with its own factors B_{GE} and Φ_{GE} , and $K_{GE}(T) = 1$.

The uniform spin liquid state of RVB type in a standard $s = 1/2$ Heisenberg model is described in terms of correlators^{12,13}

$$\Delta = \sum_{\sigma} \langle f_{i\sigma}^\dagger f_{i'\sigma} \rangle, \quad i \neq i'. \quad (14)$$

It was shown in Ref. 14 that the weak-coupling Kondo interaction at $T > T_K$ favors the stabilization of RVB state against antiferromagnetic ordering because the Kondo scattering screens the local moment leaving intact the singlet RVB correlators (14). This stabilization ‘‘quenches’’ the Kondo scattering at temperatures $T \sim T^* > T_K$ and allows the description of spin liquid in terms of RVB correlation functions at $T < T_K$, since T_K is no more a singular point of perturbation theory. Having in mind this stabilization mechanism we use the mean-field approximation for the uniform RVB state even at $T < T_K$. Although the interaction with ‘‘slow’’ conduction electrons and the influence of spin and gauge fluctuations can modify the properties of spin fermions, we use this mean-field description as the basic approximation for studying the system with the CF excitations involved.

Thus, the correlator similar to Eq. (14) can be introduced for the ground state doublet $G\nu$:

$$\Delta^G = \sum_{\nu} \langle f_{iG\nu}^\dagger f_{i'G\nu} \rangle, \quad i \neq i'. \quad (15)$$

The spin-fermion excitations which are described by the Hamiltonian (10) are constrained by the condition

$$\sum_{\Lambda} f_{i\Lambda}^\dagger f_{i\Lambda} = 1. \quad (16)$$

Important contributions to the interplay between the low-energy spinon excitations and the one-site CF excitations are connected with the interactions H' which appear in the Hamiltonian (2) beyond CC approximation. The origin of these interactions is the hybridization $\bar{V}_{k\Lambda}^{\Lambda'} = \langle \mathbf{i}\Lambda | V' | k\Lambda' \rangle$ where V' is the component of the crystal field which has the symmetry *lower* than that diagonalizing the energy terms E_{Γ} . When the integrals $\bar{V}_{k\Lambda}^{\Lambda'}$ are included in the canonical transformation, additional effective exchange terms appear:

$$H'_{\text{ex}} = \sum_{kk'} \sum_{\mathbf{i}, E, \nu\nu', \nu''} [(\bar{V}_{kG}^{E*} V_{k'G}^i)(\epsilon_k - E_f)^{-1} f_{iE\nu}^\dagger f_{iG\nu'} c_{k'G\nu'}^+ c_{kG\nu''} + (V_{kG}^{i*} \bar{V}_{k'E}^{IG})(\epsilon_k - E_f)^{-1} f_{iG\nu}^\dagger f_{iG\nu'} c_{k'E\nu''}^+ c_{kG\nu} + \text{H.c.}]. \quad (17)$$

These terms being combined with CC exchange term (7) gives additional contributions to the intersite effective exchange, and the first-order terms in \bar{V} have the following form:

$$\bar{H}_{\text{RKKY}}^{(nd)} = \sum_{\mathbf{i}\mathbf{i}'} \sum_{E\nu\nu'\nu''} [\bar{I}_{\mathbf{i}\mathbf{i}'}^{GE} f_{iG\nu}^\dagger f_{iE\nu'} f_{i'E\nu''}^\dagger f_{i'G\nu''} + \text{H.c.}]. \quad (18)$$

Here $\bar{I}_{\mathbf{i}\mathbf{i}'}^{GE}$ is the integral of the same type as that in Eq.

(13), but the corresponding coupling constant $(\alpha')^2$ is proportional to $V^3 \bar{V}$ and the factors \bar{B}_{GE} and $\bar{K}(T)$ differ from those in Eq. (13).

Then, introducing the correlator Δ^G (15), we obtain the mean-field Hamiltonian for the spin-fermion spectrum. [The nondiagonal term (12) gives no contribution to the uniform mean-field RVB pairing and describes only the fluctuation corrections to the mean-field solutions. These corrections are beyond the framework of the present paper:]

$$H_{\text{MF}} = \widetilde{E}_G \sum_{\mathbf{i}, \nu} f_{\mathbf{i}G\nu}^\dagger f_{\mathbf{i}G\nu} + \sum_{\mathbf{i} \neq \mathbf{i}'} \sum_{\nu} \mathcal{T}_{\mathbf{i}\mathbf{i}'} f_{\mathbf{i}G\nu}^\dagger f_{\mathbf{i}'G\nu} + \delta H_{\text{MF}}, \quad (19)$$

where

$$\begin{aligned} \delta H_{\text{MF}} = & \widetilde{\Delta}_{\text{CF}} \sum_{\mathbf{i}\nu} f_{\mathbf{i}E\nu}^\dagger f_{\mathbf{i}E\nu} + \sum_{\mathbf{i}\nu\nu'} [\mathcal{B}_{\mathbf{i}\mathbf{i}}^{GE} f_{\mathbf{i}G\nu}^\dagger f_{\mathbf{i}E\nu'} + \text{H.c.}] \\ & + \sum_{\mathbf{i} \neq \mathbf{i}'} \sum_{\nu\nu'} [\mathcal{B}_{\mathbf{i}\mathbf{i}'}^{GE} f_{\mathbf{i}G\nu}^\dagger f_{\mathbf{i}'E\nu'} + \text{H.c.}]. \end{aligned} \quad (20)$$

We use the bare ground state CF level as a reference point, $E_G = 0$, then

$$\widetilde{E}_G = -N^{-1} \sum_{\mathbf{k}, \mathbf{k} > k_F} J_{\mathbf{i}}^{GG}(\mathbf{k}, \mathbf{k}) + \sum_{\mathbf{i}' \neq \mathbf{i}} I_{\mathbf{i}\mathbf{i}'}^{GG} \equiv B_c^G + B_{\text{ex}}^G \quad (21)$$

includes the covalent and indirect exchange contribution to CF shift determined by the interactions (8) and (11), respectively, and

$$\widetilde{\Delta}_{\text{CF}} = \Delta_{\text{CF}} - N^{-1} \sum_{\mathbf{k}, \mathbf{k} > k_F} J_{\mathbf{i}}^{EE}(\mathbf{k}, \mathbf{k}) \equiv B_c^E \quad (22)$$

also includes the one-site covalent corrections. The coupling constant in the MF Hamiltonian is given by the following equation:

$$\mathcal{T}_{\mathbf{i}\mathbf{i}'} = \sum_{\nu} I_{\mathbf{i}\mathbf{i}'}^{GG} \langle f_{\mathbf{i}G\nu}^\dagger f_{\mathbf{i}'G\nu} \rangle = I_{\mathbf{i}\mathbf{i}'}^{GG} \Delta^G. \quad (23)$$

Only the sites connected by antiferromagnetic RKKY coupling contribute to the RVB correlation function.

The one-site and intersite mixing constants are determined as

$$\mathcal{B}_{\mathbf{i}\mathbf{i}'}^{GE} = - \sum_{\mathbf{k} > k_F} \frac{\overline{V}_{kG}^{E*} V_{kG}^i}{\epsilon_k - E_f} \quad (24)$$

and

$$\mathcal{B}_{\mathbf{i}\mathbf{i}'}^{GE} = \overline{I}_{\mathbf{i}\mathbf{i}'}^{GE} \Delta^G, \quad (25)$$

respectively.

Then, one should diagonalize the quadratic form (19) and (20) and obtain the spinon dispersion law $\varepsilon_{\beta}(\mathbf{k})$ (β are the indices of spinon band) under the global constraint condition

$$(2N)^{-1} \sum_{\mathbf{k}, \beta} \left(1 - \tanh \frac{\varepsilon_{\beta}(\mathbf{k}) - \mu}{2T} \right) = 1, \quad (26)$$

which is used in the mean-field approximation instead of exact local constraint (16). This equation determines the spinon chemical potential μ .

Thus, to find the spin-fermion spectrum in the mean-field approximation we need only to diagonalize the Hamiltonian (19) and (20) under the constraint (26).

III. SPINON SPECTRUM OF CeNiSn

CeNiSn crystallizes in the orthorhombic lattice which belongs to the noncentrosymmetric space group $Pn2_1a$.¹⁸ This

structure can be described as zigzag chains of Ce atoms directed along the a axis (easy magnetization axis) and surrounded by slightly distorted trigonal ‘‘drums’’ formed by Ni and Sn ions. Thus, the point symmetry of the crystal field on Ce ions can be treated as nearly trigonal (D_{3d}) with rotation axis parallel to the a axis of the crystal, and the monoclinic distortion (C_s) can be considered as a small correction to the trigonal crystal field.⁴ Each elementary cell contains four Ce ions.

To apply the theory of a spin liquid state explicated in Sec. II to the case of CeNiSn, one may use the irreducible representation of the trigonal point group D_{3d} as a basis for Cornut-Coqblin model and then treat the C_s distortion as a perturbation intermixing the trigonal CF terms. It was proposed in Ref. 2 (see also Ref. 11) and then confirmed in an indirect experiment⁴ mentioned in the Introduction, that the ground state level and the first excited level form a pair of Kramers doublets

$$|G \pm\rangle = a|\pm 1/2\rangle \pm b|\mp 5/2\rangle, \quad (27)$$

$$|E \pm\rangle = |\pm 3/2\rangle, \quad (28)$$

separated by small energy interval which was estimated as ≈ 4.4 meV in a point charge approximation for the crystal field. Indeed, the purely electrostatic approximation is crude enough, because the covalent and exchange corrections should be taken into account as it is seen from our Eqs. (21) and (22). These corrections result in additional reduction of the CF splitting (see below), so one can be sure that the third CF level is high enough in energy (≈ 14.0 meV according to calculations of Ref. 4), and the latter state is irrelevant to the low-energy excitation spectrum.

To calculate the spectrum of RVB excitations one should diagonalize the mean-field Hamiltonian $H_{\text{MF}} + \delta H_{\text{MF}}$ given by Eqs. (19) and (20) by means of a Fourier transformation in a Ce sublattice which, in turn, has four sublattices in this orthorhombic structure with the use of the basis functions (27) and (28). This is a cumbersome procedure in a general case, but in the special case of CeNiSn one should take into account the extreme anisotropy of the magnetic response which is seen both in static magnetic susceptibility³ and in the quasi-2D character of neutron scattering spectra.^{7,8} These experimental facts enabled us to presume that the magnetic anisotropy reflects the quasi-2D character of low-energy spin excitations and, hence, to consider the physical situation when these excitations possess the dispersion only in the bc plane. The 2D character of spin-fermion excitations can be explained by the properties of the indirect RKKY interaction which is responsible for spinon coupling. It is obvious that only those spins can be involved in the resonating valence bond which are connected by the antiferromagnetic exchange coupling. If one adopts the positive sign of the integral $I_{\mathbf{i}, \mathbf{i}+\rho}^{GG}$ in the bc plane (ρ is the distance between nn Ce ions), one can easily imagine that a 15% lesser value of intersite distance in the a direction¹⁸ is enough to have a nearly zero or even negative value of oscillating function $\Phi(\mathbf{k}_F, \mathbf{R}_i - \mathbf{R}_{i+\rho})$ in the integral (13). One should emphasize that this assumption does not imply two dimensionality of a conduction electron spectrum which can hardly be imagined in a CeNiSn lattice.

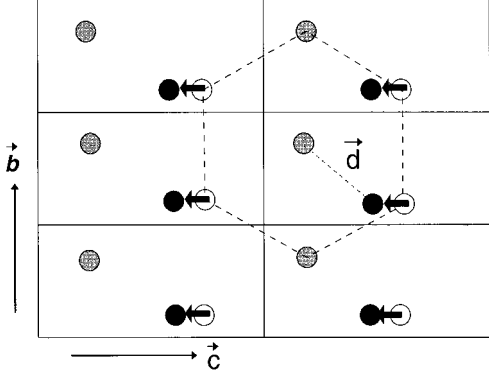


FIG. 1. The bc plane of the CeNiSn lattice. Two Ce sublattices are denoted by black and grey circles, respectively. The orthorhombic distortion \mathcal{O} (solid arrows) transforms the simple hexagonal lattice into a two-sublattice orthorhombic one. The vector \mathbf{d} is the basis vector of a two-ion elementary cell.

Another possible source of anisotropy of a magnetic excitation spectrum is the anisotropy of indirect exchange described by the factor $B_G(\theta, \phi)$ in Eq. (13). The degree of anisotropy given by this mechanism can be estimated for a special case of the ground state (27) (see the Appendix). This estimation shows that the ‘‘in plane’’ interaction exceeds the interaction along the a axis when $|a| \gg |b|$ in the case of small interionic distances and when $|a| \ll |b|$ in the case of great interionic spaces. Since the interionic distance in CeNiSn is neither big nor small and the experimental value of a can be estimated as $a \approx 0.67$ (see below), we have no real grounds for referring to this mechanism.

One more reason for changing the sign of Φ is the anisotropy of the electron Fermi surface. However, the available information about the latter is rather scanty, so we have no firm basis for discussing this mechanism.

In any case the assumption of two-dimensionality is not crucial for the results obtained, as soon as the exchange interaction along the a direction is not too big. The brief analysis of the influence of the a component of spinon dispersion on the neutron scattering spectra is presented in Sec. V D.

Thus, assuming the 2D dispersion of spin liquid excitations, we project the Ce sublattice onto the bc plane and find that the orthorhombic 2D elementary cell contains two Ce ions in the sites $\mathbf{i} = I\xi$ where $\xi = 1, 2$ defines the sublattice (see Fig. 1). This network is defined by the Bravais vectors $\mathbf{B} = (b, 0)$ and $\mathbf{C} = (0, c)$ and the basis vector $\mathbf{d} = (0, -b/2, c/2 - \mathcal{O})$. Here \mathcal{O} is the orthorhombic distortion which transforms a one-ion hexagonal lattice into a two-ion orthorhombic one.

To describe the 2D spinon spectrum in a nearest neighbor approximation we define the coupling constants $\mathcal{T}_{\mathbf{i}\mathbf{i}'}$ in Eq. (23) by two parameters,

$$\mathcal{T}_1 = \mathcal{T}_{11,1'1} = \mathcal{T}_{22,1'2} \quad (29)$$

for coupling within the same sublattice, and

$$\mathcal{T}_2 = \mathcal{T}_{11,1'2} = \mathcal{T}_{22,1'1} \quad (30)$$

for intersublattice coupling. Similarly, two mixing integrals $\mathcal{B}_{\mathbf{i}\mathbf{i}'}$ in Eq. (24) are introduced, i.e., the one-site coupling

constant (this constant also includes the contribution of monoclinic distortion of an electrostatic crystal field)

$$\mathcal{G}_1 = \mathcal{B}_{11,11}^{GE} = \mathcal{B}_{22,22}^{GE} \quad (31)$$

and intersite coupling constant

$$\mathcal{G}_2 = \mathcal{B}_{11,1'2}^{GE} = \mathcal{B}_{22,1'1}^{GE}. \quad (32)$$

Such a choice implies that the very existence of two sublattices is due to the orthorhombic distortion \mathcal{O} of a trigonal lattice, so the displacement of a second sublattice (see Fig. 1) is, probably, the main source of the non-Coqblin hybridization. Then, introducing the Fourier transformation of a spinon operator,

$$f_{\mathbf{k}\mu} = N^{-1/2} \sum_I \sum_{\xi=1}^2 \sum_{\Gamma}^{G,E} \sum_{\nu}^{\pm} \Xi_{\mu}^{\Gamma,\nu}(\xi, \mathbf{k}) f_{I\xi, \Gamma\nu} \exp(i\mathbf{k}I) \quad (33)$$

and taking into account the fact that this type of displacement generates the crystal field, the components of which are given by the Stevens operators \hat{O}_n^2 (see also Sec. V B), we find the system of equations for the coefficients $\Xi_{\mu}^{\Gamma,\nu}(\xi, \mathbf{k})$ and eigenvalues $\varepsilon_{\mu}(\mathbf{k})$,

$$\sum_{I'}^N \sum_{\xi'=1}^2 \sum_{\Gamma'}^{G,E} \sum_{\nu'}^{\pm} D_{\Gamma'\Gamma'}^{\xi\xi'}(\mathbf{R}_{II'}) \Xi_{\mu}^{\Gamma',\nu'}(\xi', \mathbf{k}) \exp\{i\mathbf{k}I'\} = \varepsilon_{\mu}(\mathbf{k}) \Xi_{\mu}^{\Gamma,\nu}(\xi, \mathbf{k}) \exp\{i\mathbf{k}I\}. \quad (34)$$

Here the coefficients $D_{\Gamma'\Gamma'}^{\xi\xi'}(\mathbf{R}_{II'})$ are defined as

$$\begin{aligned} D_{EE}^{\xi\xi}(\mathbf{R}=\mathbf{0}) &= \tilde{\Delta}_{\text{CF}}, & D_{GG}^{11}(\mathbf{R}=\mathbf{R}_1) &= \mathcal{T}_1, \\ D_{GG}^{12}(\mathbf{R}=\mathbf{R}_1) &= \mathcal{T}_2, & D_{EG}^{11}(\mathbf{R}=\mathbf{0}) &= \mathcal{G}_1, \\ D_{EG}^{12}(\mathbf{R}=\mathbf{R}_1) &= \mathcal{G}_2 \end{aligned} \quad (35)$$

[see Eqs. (29)–(32)], \mathbf{R}_1 is the coordinate of the nearest neighboring site. Then the secular matrix can be decoupled into two blocks, $\{(1G+), (2G+), (1E-), (2E-)\}$ and $\{(1G-), (2G-), (1E+), (2E+)\}$ which correspond to two new Kramers doublets given by the following linear combinations:

$$\begin{aligned} f_{\mathbf{k}\mu, \pm} &= \Xi_{\mu}^G(1, \mathbf{k}) f_{\mathbf{k}1, G\pm} + \Xi_{\mu}^G(2, \mathbf{k}) f_{\mathbf{k}2, G\pm} + \Xi_{\mu}^E(1, \mathbf{k}) f_{\mathbf{k}1, E\mp} \\ &+ \Xi_{\mu}^E(2, \mathbf{k}) f_{\mathbf{k}2, E\mp}. \end{aligned} \quad (36)$$

Each block of the secular matrix has the form

$$\begin{pmatrix} \mathcal{T}_1 M_1(\mathbf{k}) & \mathcal{T}_2 M_2(\mathbf{k}) & \mathcal{G}_1 & \mathcal{G}_2 M_2(\mathbf{k}) \\ \mathcal{T}_2 M_2^*(\mathbf{k}) & \mathcal{T}_1 M_1(\mathbf{k}) & \mathcal{G}_2 M_2^*(\mathbf{k}) & \mathcal{G}_1 \\ \mathcal{G}_1 & \mathcal{G}_2 M_2(\mathbf{k}) & \tilde{\Delta}_{\text{CF}} & 0 \\ \mathcal{G}_2 M_2^*(\mathbf{k}) & \mathcal{G}_1 & 0 & \tilde{\Delta}_{\text{CF}} \end{pmatrix}. \quad (37)$$

The structure factors which define the spinon dispersion are determined as

$$M_1(\mathbf{k}) = 2 \cos(\mathbf{k}\mathbf{B}), \quad (38)$$

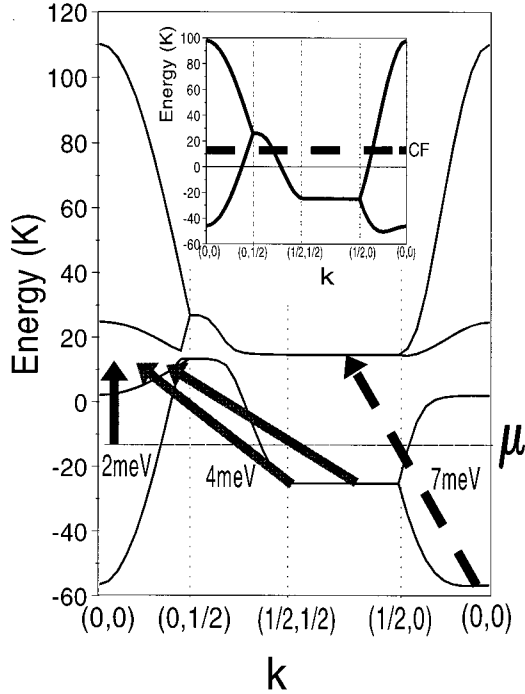


FIG. 2. The spinon dispersion in CeNiSn along the high symmetry directions of a 2D Brillouin zone obtained for the following parameter values (in K) of the secular matrix (37): $\mathcal{T}_1 = 12.7$, $\mathcal{T}_2 = 18.0$, $\tilde{\Delta}_{\text{CF}} = 13.5$, $\mathcal{G}_1 = 3.5$, $\mathcal{G}_2 = 7.7$. A horizontal line at the energy $E = -13$ K is the Fermi level position at $T = 0$. The arrows indicate the intraband and interband transitions responsible for the main peaks in a neutron scattering cross section (see text). Inset: the nonhybridized spinon spectrum with a CF level (dashed line) superimposed.

$$M_2(\mathbf{k}) = 4 \exp\left(i \frac{\mathbf{kB} - \mathbf{kC}}{2}\right) \cos\left(\frac{\mathbf{kB}}{2}\right) \cos\left(\frac{\mathbf{kC}}{2}\right) \quad (39)$$

[$\mathbf{B} = (b, 0)$ and $\mathbf{C} = (0, c)$].

The excitation spectrum is shown in Fig. 2 [the inset presents the dispersion of spin excitations in Coqblin-Cornut approximation ($\mathcal{G}_1 = 0, \mathcal{G}_2 = 0$) where the CF excitations are simply superimposed on the ground state spinon band]. It is seen from this figure that the intermixing of spinon and CF excitations results in radical reconstruction of the low-energy part of this spectrum. We associate the characteristic temperature T^* estimated from various experiments as $T^* \approx 80$ K (see the Introduction) with the characteristic energy scale of this structured part, so the values of $\mathcal{T}_1 = 18$ K and $\mathcal{T}_2 = 12.7$ K were chosen to reproduce approximately the width of this energy interval. The values of other parameters (\mathcal{G}_1 , \mathcal{G}_2 , and $\tilde{\Delta}_{\text{CF}}$) were taken to fit the positions of the main peaks in the neutron scattering spectra (see the next section). In particular, we adopted the value of 13.5 K for the renormalized CF splitting parameter $\tilde{\Delta}_{\text{CF}}$. Its reduction in comparison with the value of 48.4 K given by indirect experiment of Ref. 4 is easily explained by the effects of covalent and exchange renormalization given by the terms B_c^G , B_c^E , and B_{ex}^G in Eqs. (21) and (22). It is obvious that the covalent repulsion B_c^G of the localized levels E_Γ from the free conduction band states above the Fermi level (21) and (22) is

governed by the value of hybridization matrix elements $|V_{k\Gamma}^i|^2$. Since the Fermi surface of CeNiSn is dominated by the p -partial waves,²⁰ the hybridization is largest for the $j_z = \pm 1/2$ and $j_z = \pm 3/2$ components of the f states. Therefore, the ratio of hybridization matrix elements for $|G \pm\rangle$ (27) and $|E \pm\rangle$ (28) can be evaluated as $|V_{kG\pm}^i|^2 / |V_{kE\pm}^i|^2 \approx a^2 < 1$. This means that the *negative* covalent term reduces the CF splitting. The exchange contribution B_{ex}^G in Eq. (21) gives an additional contribution to this reduction effect.

The dispersionless behavior of the spinon spectrum at the b facet of the Brillouin zone [$(0, 1/2, 0) \leq \mathbf{k} \leq (0, 1/2, 1/2)$] is explained by the specific form of the spinon spectrum

$$\varepsilon_{\mu=1,2}(\mathbf{k}) = 2 \left\{ \mathcal{T}_1 \cos(\mathbf{kB}) \pm 2 \mathcal{T}_2 \cos\left(\frac{\mathbf{kB}}{2}\right) \cos\left(\frac{\mathbf{kC}}{2}\right) \right\} \quad (40)$$

since this spectrum becomes dispersionless for $\mathbf{kB} = \pi$.

It is important that inclusion of intermixing terms $\mathcal{G}_{1,2}$ in the secular matrix (37) does not alter the one-dimensionality of this branch (cf. upper and lower panels of Fig. 2) because the form factor M_2 given by Eq. (39) also turns into zero at $\mathbf{kB} = \pi$. Based on the spinon dispersion law shown in this picture we will try in the next section to explain the neutron scattering data. The chemical potential of spin fermions at $T = 0$ which is determined by the constraint (26) is shown in this picture by the dashed line.

Thus we find that the spin excitations in CeNiSn preserve to some extent the features of the one-site crystal-field excitation spectrum: the multiband dispersion picture contains vast dispersionless parts whose origin is the initial atomic crystal-field splitting of the f level. The density of spin-fermion states described by these bands is shown in the upper and lower panels of Fig. 3. We see that instead of a simple two-level picture of CF excitations there exists several peaks, some of which can be considered as the remnants of CF levels but others reflect the van Hove singularities of a 2D spinon spectrum. The spectrum demonstrates the pseudogap features presupposed in early phenomenological descriptions.³ However, it is remarkable that the chemical potential of spin-fermion excitations falls not into the hybridization gap but into the pseudogap between two van Hove peaks.

IV. INELASTIC NEUTRON SCATTERING IN SPIN LIQUID

The inelastic neutron scattering provides unique experimental information concerning the structure and dispersion of low-energy spin excitations, so these data look challenging for the general theory of the spin liquid and especially for the case of interplay between HF and CF excitations. To calculate the spectra of inelastic neutron scattering in the spin liquid, we start with the well-known equation for magnetic scattering cross section

$$\frac{d^2\sigma}{d\Omega dE'} = \left(\frac{\gamma e^2}{m_e c^2}\right)^2 \frac{\kappa'}{\kappa} \sum_{\alpha\beta} (\delta_{\alpha\beta} - \hat{Q}_\alpha \hat{Q}_\beta) S_{\alpha\beta}(\mathbf{Q}, \hbar\omega). \quad (41)$$

Here m_e and e are the mass and the charge of electron, $\gamma = -1.91$ is the gyromagnetic ratio for neutron, c is the light velocity. The wave vectors κ and κ' are momenta of incident and scattered neutrons, respectively, and \hat{Q}_α are the Cartesian components of the unit vector directed along the momentum transfer vector \mathbf{Q} . The component $S_{\alpha\beta}(\mathbf{Q}, \hbar\omega)$ of the scattering function can be expressed as the sum over all possible initial (λ) and final (λ') states with the energies E_λ and $E_{\lambda'}$, respectively,

$$S_{\alpha\beta}(\mathbf{Q}, \hbar\omega) = \sum_{\lambda\lambda'} n_\lambda \langle \lambda | \hat{Q}_\alpha^+ | \lambda' \rangle \langle \lambda' | \hat{Q}_\beta | \lambda \rangle \delta(\hbar\omega + E_\lambda - E_{\lambda'}) \quad (42)$$

(n_λ is the probability distribution for initial state). Then, the operator \hat{Q} of neutron-electron interaction can be expressed as a sum over all f ions,

$$\hat{Q} = \sum_f \exp(i\mathbf{Q}\mathbf{R}_f) \sum_\xi^{\text{cell}} \exp(i\mathbf{Q}\mathbf{d}_\xi) \hat{Q}_{f\xi}. \quad (43)$$

In the dipolar approximation the operator $\hat{Q}_{f\xi}$ turns into

$$\hat{Q}_{f\xi} = \frac{1}{2} g F(\mathbf{Q}) \hat{\mathbf{J}}_{f\xi}, \quad (44)$$

where g is the Lande splitting factor, $F(\mathbf{Q})$ is the ionic form factor, and $\hat{\mathbf{J}}$ is the total angular momentum operator. Thus the problem is reduced to calculation of the correlator $\langle \lambda | \hat{J}_{f\xi}^+ \hat{J}_{f'\xi'}^- | \lambda \rangle$.

In our model the source of neutron scattering is the transitions between the spin liquid excitations described by the operators (33) with the dispersion law $\varepsilon_\mu(\mathbf{k})$ given by the secular equation (37). Now the situation formally resembles the well-known paramagnetic scattering¹⁹ where the spin-fermion excitations $\lambda = \mathbf{k}\mu$ play the same part as the itinerant electrons in transition metals. Substituting the eigenvectors given by Eq. (33) in the scattering function (42), we find

$$S_{\alpha\beta}(\mathbf{Q}, \hbar\omega) = [\frac{1}{2} g F(\mathbf{Q})]^2 \sum_{\mu\mu'} \sum_{\mathbf{k}} [I_\alpha^{\mu\mu'}(\mathbf{k}, \mathbf{Q})]^* I_\beta^{\mu\mu'}(\mathbf{k}, \mathbf{Q}) n_\mu(\mathbf{k}) [1 - n_{\mu'}(\mathbf{k} - \mathbf{Q})] \delta[\hbar\omega + \varepsilon_\mu(\mathbf{k}) - \varepsilon_{\mu'}(\mathbf{k} - \mathbf{Q})], \quad (45)$$

where

$$I_\alpha^{\mu\mu'}(\mathbf{k}, \mathbf{Q}) = \sum_{\Gamma\nu} \sum_{\Gamma'\nu'} \sum_\xi \exp(i\mathbf{Q}\mathbf{d}_\xi) (\Xi_\mu^{\Gamma,\nu}(\xi, \mathbf{k}))^* \Xi_{\mu'}^{\Gamma',\nu'}(\xi, \mathbf{k} - \mathbf{Q}) \langle \Gamma\nu | \hat{J}^\alpha | \Gamma'\nu' \rangle. \quad (46)$$

$n_\mu(\mathbf{k})$ is the Fermi distribution function for spinon excitations.

This expression can be simplified in case of CeNiSn. It is known from experiment^{9,10} that the dominant component which contributes significantly to the scattering function is the $S_{aa}(\mathbf{Q}, \hbar\omega)$ component. Thus, for the momentum transfer \mathbf{Q} in the b - c plane, which is the experimental condition for most of the experimental scans, one has for the scattering function

$$S_{aa}(\mathbf{Q}, \hbar\omega) = [\frac{1}{2} g F(\mathbf{Q})]^2 \sum_{\mu\mu'} \sum_{\mathbf{k}} |I_a^{\mu\mu'}(\mathbf{k}, \mathbf{Q})|^2 n_\mu(\mathbf{k}) [1 - n_{\mu'}(\mathbf{k} - \mathbf{Q})] \delta[\hbar\omega + \varepsilon_\mu(\mathbf{k}) - \varepsilon_{\mu'}(\mathbf{k} - \mathbf{Q})]. \quad (47)$$

Since the a axis is the axis of spin quantization, and since the operator J_a has only diagonal nonzero matrix elements in the basis of CF states, $|\Gamma\nu\rangle$ (27) and (28), the expression for $I_a^{\mu\mu'}(\mathbf{k}, \mathbf{Q})$ has the form

$$I_a^{\mu\mu'}(\mathbf{k}, \mathbf{Q}) = \sum_{\Gamma\nu} \sum_\xi \exp(i\mathbf{Q}\mathbf{d}_\xi) [\Xi_\mu^{\Gamma,\nu}(\xi, \mathbf{k})]^* \Xi_{\mu'}^{\Gamma,\nu}(\xi, \mathbf{k} - \mathbf{Q}) \langle \Gamma\nu | \hat{J}^a | \Gamma\nu \rangle. \quad (48)$$

Finally, taking into account the explicit equation (36) for the spin operator and expressions for the CF states (27) and (28), one comes to the final equation for the matrix element $I_{\alpha\pm}^{\mu\mu'}(\mathbf{k}, \mathbf{Q})$ [\pm signs are for up and down partners of the Kramers doublet (36), respectively]:

$$I_{\alpha\pm}^{\mu\mu'}(\mathbf{k}, \mathbf{Q}) = \{ [\Xi_\mu^G(1, \mathbf{k})]^* \Xi_{\mu'}^G(1, \mathbf{k} - \mathbf{Q}) \Theta_{G\pm} + [\Xi_\mu^E(1, \mathbf{k})]^* \Xi_{\mu'}^E(1, \mathbf{k} - \mathbf{Q}) \Theta_{E\mp} \} + \{ [\Xi_\mu^G(2, \mathbf{k})]^* \Xi_{\mu'}^G(2, \mathbf{k} - \mathbf{Q}) \Theta_{G\pm} + [\Xi_\mu^E(2, \mathbf{k})]^* \Xi_{\mu'}^E(2, \mathbf{k} - \mathbf{Q}) \Theta_{E\mp} \} \exp(i\mathbf{Q}\mathbf{d}), \quad (49)$$

where

$$\Theta_{G\pm} = \pm \left(3a^2 - \frac{5}{2} \right), \quad (50)$$

$$\Theta_{E\pm} = \pm \frac{3}{2}. \quad (51)$$

V. INELASTIC NEUTRON SCATTERING SPECTRA IN CeNiSn

In this section we compare the inelastic neutron scattering spectra calculated by means of Eqs. (47) and (49) with the dispersion law for spin fermions given by the secular matrix (37) and Fig. 2 with the experimental data of Refs. 7–10.

A. Qualitative considerations

The inelastic neutron scattering spectrum of CeNiSn in its gross features is formed by two main signals with energies of ~ 2 and ~ 4 meV. It is seen from the lower panels of Figs. 2 and 3 that these ‘‘peaks’’ can be ascribed to transitions from the occupied states in the lower band to the region of the empty levels where the states $|G\pm\rangle$ (27) and $|E\pm\rangle$ (28) are strongly hybridized. The most distinctly these features are seen in experiment for the momentum transfer vector \mathbf{Q} in the bc plane and, hence, the magnetic response is connected with the χ^{aa} component of dynamic magnetic susceptibility.⁹ As is known from the measurements of static susceptibility, the a axis is the easy magnetization axis in CeNiSn.³ Since the lower spinon band is formed mainly by the ground state doublet $|G\pm\rangle$ (27) where the components $|\pm 5/2\rangle$ play the main part (see the next subsection), the longitudinal susceptibility should be the strongest component of the magnetic response at low energies, so the dominance of the $\mathbf{Q}\perp a$ momentum transfer vectors is naturally explained in our model. Then the most intense transitions are expected for those final states where the greater fraction of $|\pm 5/2\rangle$ is admixed to the $|\pm 3/2\rangle$ states.

The 2 meV peaks are seen experimentally for $\mathbf{Q}=(0,0,1)$ (Ref. 7) and $\mathbf{Q}=(0,1,0)$.^{8,9} The corresponding momentum transfer vectors are indicated by solid arrows in Fig. 4 where the shaded area is the projection of Brillouin zone to the bc plane. These processes correspond to the vertical transitions from the spinon ‘‘Fermi surface’’ to the region of strong hybridization near the point $\mathbf{k}=(0,0,1/2)$. The bold arrow marks these transitions in Fig. 2 [the integer reciprocal vectors (0,1,0) or (0,0,1) are subtracted]. The same transitions are shown by the bold arrow in the lower panel of Fig. 3. The highest peak in the DOS arises due to the van Hove singularities near the former CF excitation level.

The peaks at $E=4$ meV are seen for $\mathbf{Q}=(0,1/2+n, Q_c)$ (grey arrows in Fig. 4) where n are integer numbers.^{8,9} This maximum in the scattering cross section is due to the intraband transitions shown by grey arrows in Fig. 2. It is easily seen that since the 4 meV peak corresponds to the transitions between two peaks of DOS (grey arrow in the lower panel of Fig. 3), and the 2 meV processes are due to the transitions from the structureless part of DOS to the empty peak, the

intensity of the former signal should be higher than that of the latter one. This result is also consistent with the experimental data.^{8,9}

It worth noting that the general shape of the DOS in the lower band reminds one of the double-peak DOS with the pseudogap postulated in early phenomenological models.^{3,2,6} However, at least *one more* peak with higher energy should exist in the scattering spectrum given by the present model. This peak is formed by the interband transitions shown by the dashed lines in Figs. 2 and 3. Such a peak with $E\approx 7$ meV was found in the recent neutron scattering experiments.¹⁰

Thus, the present model explains all qualitative features of the neutron scattering spectrum. To make the detailed quantitative description of experimental scans one should first specify the model parameters.

B. Evaluation of the model parameters

To calculate the spinon spectrum determined by the secular matrix (37) one should know the values of the intersite coupling constant $\mathcal{T}_{1,2}$, the mixing parameters $\mathcal{G}_{1,2}$ the energy $\tilde{\Delta}_{\text{CF}}$ of CF splitting. To find the intensities of neutron scattering one needs also the magnitude of the orthorhombic distortion \mathcal{O} and the values of parameters a, b which determine the structure of the ground state CF level $|G\pm\rangle$ (27). All these quantities, except hybridization parameters \mathcal{G}_{bc} and \mathcal{G}_0 are, indeed, predetermined by the experimental data available. The criteria for choosing the parameters $\mathcal{T}_{1,2}$ and $\tilde{\Delta}_{\text{CF}}$ are described in Sec. III. The value of orthorhombic distortion \mathcal{O} in units of lattice parameter c is 0.10.¹⁸

We have no independent experimental information to choose the values of mixing parameters $\mathcal{G}_{1,2}$, so we use these parameters for fitting the experimental neutron scattering cross section. The best values, which gave us the possibility to describe the low-energy magnetic scattering function for all measured momentum transfer, are $\mathcal{G}_1=3.5$ K, $\mathcal{G}_2=7.7$ K.

To estimate the parameters a, b entering the ground state CF level wave function (27), we used the experimental data on the anisotropy of low-temperature static magnetic susceptibility at low temperatures.⁵ According to our model, this susceptibility should be mainly determined by the Pauli-like contribution of RVB excitations.

The Pauli-like contribution for the magnetic field applied along the j axis at low temperatures is proportional to the DOS of spinons $N(\varepsilon_F)$ and to the square of an effective $g_j^{(p)}$ factor of the spinon states $|\tilde{G}\pm\rangle$ at the Fermi level, $\chi_x^{(p)} \sim |g_x^{(p)}|^2 \mathcal{N}(\varepsilon_F)$ [$\mathcal{N}(\varepsilon_F)$ is the density of spinon states at the Fermi level]. The effective $g_j^{(p)}$ factor is determined as $g_j^{(p)} = 2g_j |\langle \tilde{G}\nu | \hat{J}_j | \tilde{G}\nu' \rangle|$ ($\nu = \pm$). Here $g_j=6/7$ is the Lande factor for Ce^{3+} and \hat{J}_j is the j component of total momentum operator. According to Eq. (36), the spinon states at the Fermi surface which determine the anisotropy of the susceptibility are described as the mixture of the bare wave functions $|G\pm\rangle$ and $|E\pm\rangle$ (27) and (28) due to orthorhombic distortion of the trigonal lattice. As was mentioned above, we consider the \hat{O}_n^2 orthorhombic distortion (see Fig. 1). Therefore, the wave functions in the vicinity of the Fermi surface can be approximated by

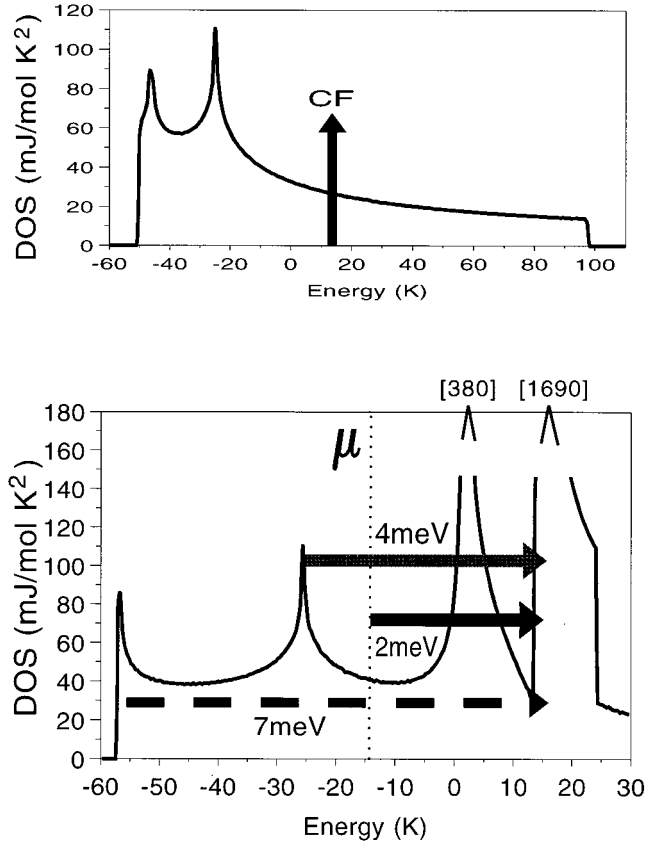


FIG. 3. Upper panel: the density of states of unhybridized spinon spectrum. Lower panel: the density of states for spin fermions hybridized with CF excitation. All other designations are the same as in Fig. 2.

$$|\tilde{G}\pm\rangle = \alpha_{av}^{(F)}|G\pm\rangle + \beta_{av}^{(F)}|E\mp\rangle, \quad (52)$$

where $\alpha_{av}^{(F)}$ and $\beta_{av}^{(F)}$ are the mixing parameters averaged over the Fermi surface.

When evaluating the Pauli contribution, we neglect the anisotropy of spinon Fermi surface and assume that the ratio between the components of static susceptibility is given by the anisotropy of the g factor:

$$\chi^a : \chi^b : \chi^c \approx |g_a|^2 : |g_b|^2 : |g_c|^2.$$

To evaluate the averaged mixing parameters $\alpha_{av}^{(F)}$ and $\beta_{av}^{(F)}$, we take into account that there are $N=4$ nearest neighbors from the second sublattice which take part in k -dependent hybridization. The averaging of the k dependence of hybridization gives an additional factor 1/2. The distance from the Fermi surface ε_F to the crystal field level is ≈ 30 K according to our calculations (see Figs. 2 and 3). Therefore, the value of β_{av} at the Fermi surface can be estimated as $\beta_{av}^{(F)} \approx NG/2(\Delta_{CF} - \varepsilon_F)$, so $\alpha_{av} \approx 0.88$. The similar value of the parameter α_{av} can be extracted from the experimental data for the anisotropy of magnetic susceptibility:

$$s_1 = \frac{|\chi_b - \chi_c|}{\chi_c} \approx \left(\frac{4\sqrt{2}\sqrt{1 - \alpha_{av}^2}}{3\alpha_{av}a} \right)^2 \quad (53)$$

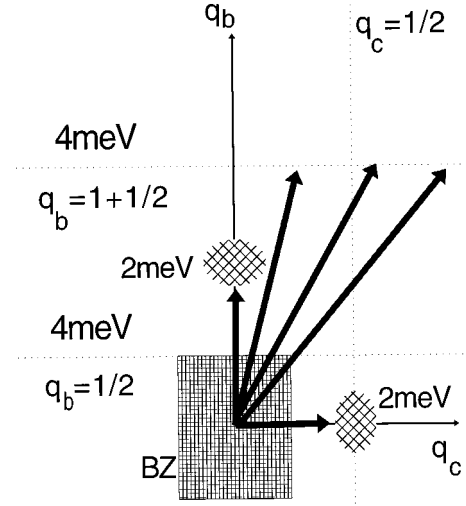


FIG. 4. The \mathbf{Q} vectors corresponding to the main transitions in the spin bands in a 2D reciprocal lattice. The shaded areas are the projection of the BZ onto bc plane and the regions in the BZ where the final states are located.

[where $s_1 \approx 0.25$ (Ref. 5)]. One finds $\alpha_{av} \approx 0.94$ from Eq. (53) in agreement with the theoretical evaluation. The estimation of the magnetic susceptibility gives

$$s_0 \equiv \frac{\chi_a}{\chi_c} \approx \frac{\chi_a}{\chi_b} \approx \left(\frac{\alpha_{av}(2 - 6a^2) + 3}{3\alpha_{av}^2 a^2} \right)^2, \quad (54)$$

where $2 < s_0 < 3$. Using Eq. (54), the value of $|a|$ is determined as

$$|a| \approx \sqrt{\frac{2\alpha_{av}^2 + 3}{3\alpha_{av}^2(2 + \sqrt{s_0})}} \quad (55)$$

so we obtain $0.65 < |a| < 0.75$. Since the contribution of the $|5/2\rangle$ component in the magnetic response is dominant even for $|a| \approx |b|$, we actually deal with the $|\pm 5/2\rangle$ states in the neutron scattering experiments. It turns out that the neutron scattering cross sections weakly depend on the value of a in the actual range of $|a|$, and we cannot extract this parameter from the available experimental data. In the following calculations, a value of $|a| = 0.67$ is taken.

C. Quantitative description of constant- \mathbf{Q} and constant- E neutron scattering scans

First, we see that our model reproduces quite well the ‘‘pseudogap’’ behavior of constant- \mathbf{Q} scans first found in Ref. 7. Figure 5 presents the theoretical curves for \mathbf{Q} perpendicular to the \mathbf{a} axis in comparison with experimental data of Ref. 7 and later results of Refs. 8 and 9. It is easily seen from Figs. 2 and 3 (lower panel) that this character of $\mathbf{Q} \perp \mathbf{a}$ scans is due to the high density of states for the $|\pm 5/2\rangle$ components in the region of strong hybridization around the $(0,0,1/2)$ point. This pseudogaplike behavior disappears for $\mathbf{Q} \parallel \mathbf{a}$ (Ref. 7) simply because the 2 meV peak is suppressed for this direction of momentum transfer in accordance with the geometrical factor in Eq. (41) under condition $\chi_{aa} \gg \chi_{bb}, \chi_{cc}$.

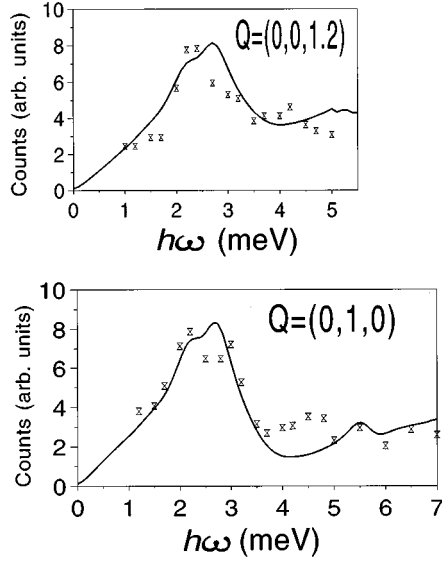


FIG. 5. Comparison of experimental (diamonds) and theoretical (curves) constant- Q scans. Upper panel: $Q=(0,0,1.2)$. Experimental points are taken from Ref. 7. Lower panel: $Q=(0,1,0)$. Experimental points are taken from Refs. 8 and 9.

The next striking feature of experimental scans is the quasi-1D character of 4 meV excitation: it was noticed^{8,9} that the behavior of this peak for $Q=(0, n+1/2, Q_c)$ practically does not depend on the value of Q_c . Our next scan demonstrates, first, that this peak indeed can be obtained in the spin-fermion model (Fig. 6, upper panel) and, second, that nothing is changed significantly in the shape of this scan with varying Q_c (lower panel). The form of the spinon dispersion curve explains this one-dimensionality: due to the dispersionless character of the energy band along the wave

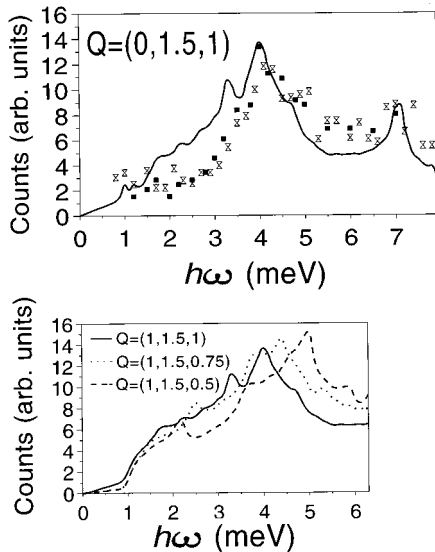


FIG. 6. Theoretical (lines) and experimental (points) constant- Q scans with a 4 meV peak. Upper panel: constant- Q scan for $Q=(0,1.5,1)$. Experimental points are taken from Refs. 8 and 9 (squares) and Ref. 10 (diamonds). Lower panel: constant- Q scans for $Q=(0,1.5,1)$ (solid line), $Q=(0,1.5,0.75)$ (dotted line), and $Q=(0,1.5,0.5)$ (dashed line).

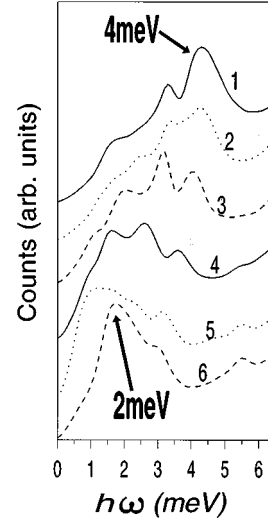


FIG. 7. Constant- Q scans for $Q=(0,1.5,0)$; $(0,1.4,0)$; $(0,1.3,0)$; $(0,1.2,0)$; $(0,1.1,0)$; $(0,1,0)$ (curves 1–6, respectively). Positions of 4 meV and 2 meV peaks are indicated by arrows. The vertical scales are shifted for clarity.

vector \mathbf{k} in the $\mathbf{k}=(0,1/2,k_c)$ direction [see Eq. (40) for explanation], the contribution from the intraband transitions with $E \sim 4$ meV to the scattering function [slanted arrows in Fig. 2(b)] does not depend on Q_c and thus mimics quasi-one-dimensional scattering.

One more remarkable property of experimental constant- Q scans is their modification along the $(0, Q_b, 0)$ direction. It was found (see Ref. 9, Fig. 3) that the form of these scans changes from the structure with a definite 4.2 meV peak at $Q_b=1.5$ to that with a 2 MeV peak at $Q_b=1$. It is seen from Fig. 7 that our theoretical scans reproduce this variation quite satisfactorily, including the featureless shape of the scan at intermediate value of $Q_b=1.2$.

The theory also explains why the 2 meV peak, which is distinctly seen for the vertical transitions $(0, Q_b, 0)$ and $(0, 0, Q_b)$ (see Figs. 4 and 5) practically disappears for the “diagonal” direction $Q=(0,1,1)$ (Fig. 6 of Ref. 9). This kind of anisotropy is explained by the fact that the phase factor $\exp(i\mathbf{Q}\mathbf{d})$ in Eq. (49) is close to unity for $Q=(0,1,1)$ due to the small orthorhombic shift $\mathcal{O}=0.10$ (see Sec. V B). Then, since the condition $\Theta_{G\pm} \approx \Theta_{E\mp}$ is valid for the choice value of $a=0.67$, the matrix element (48) and (49) practically turns out into the orthogonality relation between the different quantum states (33) with the same reduced wave vector. This is why the intensity of the scan at $Q=(0,1,1)$ is by order of magnitude smaller than that of $Q=(0,0,1)$ or $Q=(0,1,0)$.

Finally, we discuss the characteristic features of constant- E scans. The calculated scans for $E=4.2$ meV are presented in Fig. 8 together with the experimental data taken from Ref. 9. It is no wonder that the theoretical scans are in satisfactory quantitative agreement with experiment: it simply follows from the above explanation that the maxima of $(0, Q_b, 0)$ and $(0, Q_b, 1)$ scans at $Q_b=0.5, 1.5$ are connected with the fact that the 4 meV peak arises just at $Q=(0, n+1/2, x)$ with integer n and any x .

A more puzzling feature of the constant- E scans was noticed in Ref. 10 where it was observed that the peak at

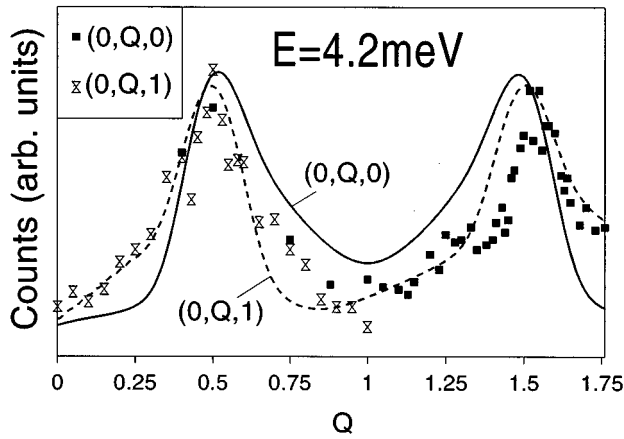


FIG. 8. Theoretical (curves) and experimental (dots) constant- E scans ($E=4.2$ meV) along $\mathbf{Q}=(0, Q_b, 0)$ (squares and solid line) and $\mathbf{Q}=(0, Q_b, 1)$ (diamonds and dashed line) directions. Experimental points are taken from Ref. 9.

$Q_b=1.5$ for the $(0, Q_b, 1)$ scans with $E=4.2$ meV splits into two peaks for lower-energy transfer $E=3.3$ meV and $E=2.5$ meV. This feature is reproduced, at least quantitatively, in our calculations (see Fig. 9). Both the appearance of the doubled peak and the increase of the splitting for lower energies is seen in the theoretical curves. Even the higher intensity of the left peak is reproduced in the calcu-

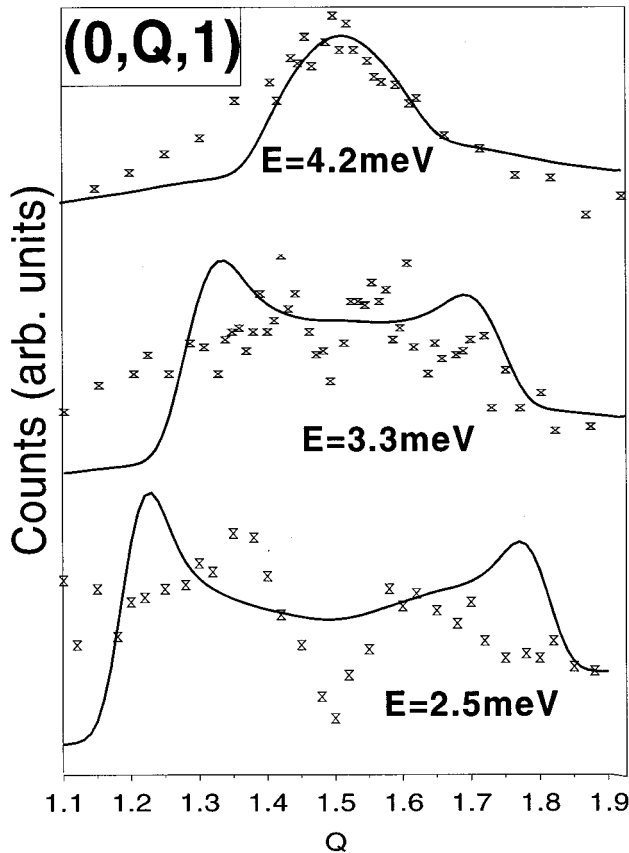


FIG. 9. Theoretical (curves) and experimental (dots) constant- E scans along the $(0, Q_b, 1)$ direction: (a) $E=4.2$ meV; (b) $E=3.3$ meV; (c) $E=2.5$ meV. Experimental points are taken from Ref. 10.

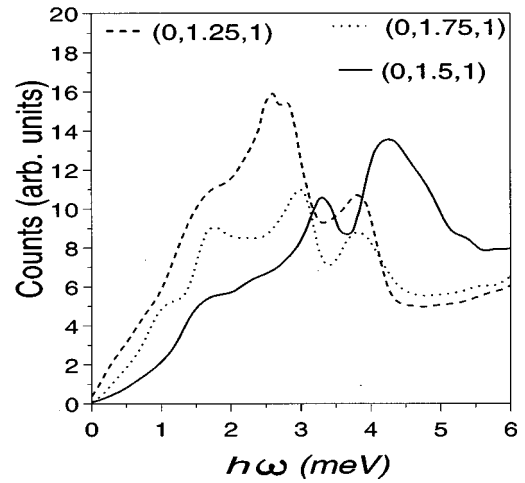


FIG. 10. Constant- \mathbf{Q} scans for $\mathbf{Q}=(0, 1.25, 1)$ (dashed line); $\mathbf{Q}=(0, 1.5, 1)$ (solid line); $\mathbf{Q}=(0, 1.75, 1)$ (dotted line).

lated scan. To investigate the reason of this asymmetry we also calculated the constant- \mathbf{Q} scans with $\mathbf{Q}=(0, Q_b, 1)$ for $Q_b=1.25, 1.5, 1.75$. Figure 10 demonstrates that for higher-energy transfer the intensity of the $Q_b=1.5$ response is higher than that of $Q_b=1.25, 1.75$, whereas for lower-energy transfer the situation is reversed.

Thus, the totality of calculated scans shows that not only the general shape but also the anisotropy of the spinon spectrum correlates with the details of experimental neutron scattering scans. These results demonstrate clearly that the anisotropic magnetic response of CeNiSn is due to the anisotropy of the spectrum of low-energy spin-fermion excitations in this system.

D. Influence of three dimensionality of the spinon spectrum

To check the robustness of our results to the assumption about the mainly two-dimensional character of spinon dispersion we recalculated the spinon DOS and inelastic neutron scattering intensities.

We introduced in the secular matrix for the spinon spectrum two more parameters, i.e., the ‘‘overlap integral’’ $T_3 = T_{11,1'3} \equiv T_{12,1'4}$ where the indices (3,4) stand for the Ce ions above and below sites (1,2), respectively, in the a direction, and $G_3 = G_{11,1'3}^{GE} \equiv G_{12,1'4}^{GE}$ with the same notations. These parameters result in further doubling of the crystal cell lattice and further removing the degeneracy of the spinon spectrum and appearance of spinon dispersion in the a direction of the Brillouin zone. As to the spinon DOS, the overlap parameter T_3 is responsible mainly for broadening of the second van Hove peak (-25 K peak in the lower panel of Fig. 3) and the influence of the hybridization parameter G_3 is seen in broadening and lowering of the 3 K peak in the mentioned DOS. But the general shape of the DOS, and, therefore, the form of the inelastic neutron scattering spectra for \mathbf{Q} in the bc plane are practically not modified at least for T_3 and G_3 less than ≈ 4 K, i.e., more than 50% of the characteristic values of in-plane interaction parameters. Correspondingly, the neutron scattering peaks for the momentum transfer in the bc plane are also slightly broadened, but the general quantitative agreement is still satisfactory, although

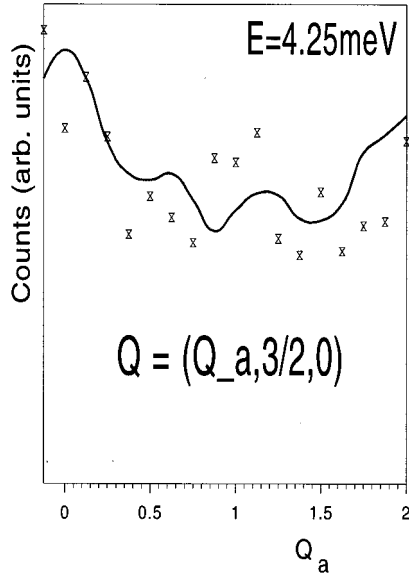


FIG. 11. Theoretical (curves) and experimental (dots) constant- E scans ($E=4.25$ meV) along the $\mathbf{Q}=(Q_a, 3/2, 0)$ direction. Experimental points are taken from Ref. 9.

the CF splitting parameter should be slightly changed. If one chooses, e.g., $T_3 = \mathcal{G}_3 = 3.5$ K, the renormalized value of $\tilde{\Delta}_{\text{CF}} = 19.5$ K should be taken to get an agreement with the experimental data for all scans demonstrated in Figs. 5–10.

However, the introduction of the third component in the spinon spectrum provided us with one more possibility to check the model assumptions, i.e., to calculate the neutron scattering for \mathbf{Q} out of the bc plane. In Fig. 11, the constant- E scan for $\mathbf{Q}=(Q_a, 3/2, 0)$ is presented in comparison with the experimental data of Ref. 9. The oscillating character of the scattering intensity with Q_a is distinctly seen in experiment and is surely reproduced in the calculated curve. It is interesting that the shape of the theoretical curve is more complicated than the rough sinusoidal guideline shown in Fig. 11(d) of Ref. 9, and the attentive look on the experimental points confirms this picture at least qualitatively.

When calculating the theoretical curve we weighted the inelastic cross section only with the form factor $F(\mathbf{Q})$ [see Eq. (45)]. This procedure resulted in better agreement with the experiment than that including also the orientational factor $1 - \hat{Q}_a^2$. This means that the contribution of $\text{Im}\chi^{bb}$ and $\text{Im}\chi^{cc}$ to this cross section is also significant due to, e.g., the zigzag distortion of Ce chains in a direction.

VI. LOW-TEMPERATURE SPECIFIC HEAT OF CeNiSn

To be sure that our approach gives a really universal description of low-energy spin excitations in CeNiSn, we calculated the magnetic contribution to specific heat of CeNiSn within the approximate mean-field approach to RVB thermodynamics with use of the same parameters for the spin-fermion spectrum which were chosen for description of the neutron scattering data.

To find the specific heat $C(T)$ at low temperatures, we calculated the average spinon energy per Ce site

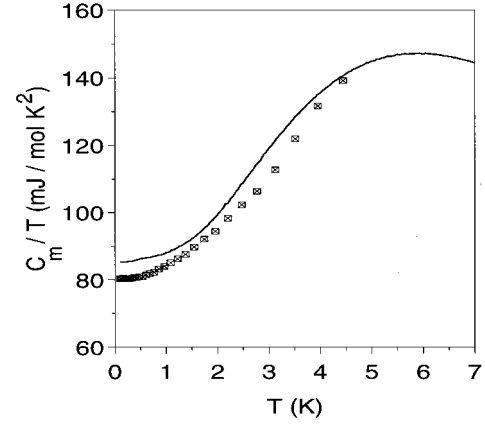


FIG. 12. Theoretical curve for the low- T contribution to the specific heat in comparison with the experimental data taken from Ref. 5 (diamonds). The constant electronic contribution $\gamma_{\text{el}} = 18$ mJ/mol K² is added to the theoretical curve (see text).

$$\mathcal{E}(T) = \frac{1}{NL} \langle H_f + H_{\text{RKKY}}^g + \bar{H}_{\text{RKKY}}^{(nd)} \rangle_{\text{spinon}}, \quad (56)$$

where $L=4$ is the number of Ce sublattices and N is the number of the elementary cells. Then, introducing the mean-field approximation of RVB type,

$$\mathcal{E}(T) = \frac{1}{NL} \sum_{i_1, i_2} \sum_{\Lambda_1, \Lambda_2} I_{i_1 i_2}^{\Lambda_1 \Lambda_2} \langle f_{i_1 \Lambda_1}^+ f_{i_2 \Lambda_2} \rangle \langle f_{i_2 \Lambda_2}^+ f_{i_1 \Lambda_1} \rangle, \quad (57)$$

we calculated these averages with the spinon spectrum defined by the parameters $T_{1,2,3}$ and $\mathcal{G}_{1,2,3}$ under global constraint (26) by using the Fourier transformation (33). The specific heat was determined as $C(T) = d\mathcal{E}(T)/dT$. This procedure gives the correct value of experimentally measured magnetic entropy $\frac{1}{4}R \ln 4$ per Ce site for $T \gtrsim \Delta_{\text{CF}}$.^{3,21}

Since the samples studied in the neutron scattering measurements, apparently, were not as perfect as the recently grown samples which demonstrate the metallic-type conductivity and low value of $\gamma = C/T \sim 40$ mJ/mol K²,⁵ we used for comparison the data for sample no. 2 from Ref. 5. The value of $\gamma(T=0.1\text{K}) = 80$ mJ/mol K² was chosen to eliminate the ultralow- T upturn due to nuclear and impurity contributions to the magnetic specific heat. The results of our calculations are presented in Fig. 12 (solid curve). The experimental data presented by diamonds in Fig. 12 are obtained from those for that sample by cancelling the phonon contribution to the specific heat. The latter was considered to be the same as in the LaNiSn crystal.²¹

When comparing the experimental and theoretical curves for the specific heat, one should take into account the contribution of conduction electrons and add it to the magnetic specific heat given by the spin-fermion excitations. We have taken it to be linear in T within the low- T interval $0 < T < 10$ K with the Sommerfeld coefficient $\gamma_e = 18$ mJ/mol K². This means that the electron contribution to the heavy-fermion density of states in good samples can be as large as $\approx 50\%$ in agreement with the theoretical predictions for the spin liquid state of the Kondo lattices.²³ It is seen from Fig. 12 that the theoretical curve describes quite well

the temperature behavior of $C/T = \gamma + bT$ at low temperature and gives the maximum of C/T at $T = 6$ K. The latter is observed for the more perfect samples²² where the data for higher temperatures are available.

It should be noted that the contribution of spinon dispersion in the a direction (see Sec. V D) practically does not change the form of the $C(T)$ curve since the van Hove peaks survive in the 3D spectrum, and the spinon chemical potential is still in the dip of the DOS.

Our previous semiphenomenological studies have shown that the model of heavy-fermion liquid with the pseudogap in the spin-fermion excitations induced by the interplay with the CF excitations describes quantitatively the low-temperature specific heat and thermal expansion of CeNiSn.^{2,11} Now we see that the consequent microscopic theory gives a detailed picture of the low-energy excitations and low-temperature thermodynamics of this system which is in reasonable quantitative agreement with the experiment.

VII. CONCLUDING REMARKS

To conclude, we have found that the general theory of spin fermions acquires some specific features in the low-symmetry Kondo lattice materials with soft CF excitations, such as CeNiSn and CeRhSb. These CF excitations modify the spectrum of spin excitations in a very characteristic manner, and as a result, the density of spin-fermion states has several peaks due to interaction between the spin-fermion excitations and CF excitations. Because of existence of these peaks the spin response of CeNiSn and CeRhSb reminds one of spin-gap materials.

Whereas the largest peak in spinon DOS at ≈ 2 meV above the spinon Fermi level appears as a result of interplay between the HF and CF excitations, all other singularities in one-spinon and two-spinon DOS arise due to quasi two-dimensionality of spin excitation spectrum (although these singularities are robust enough against the appearance of the third component of spinon dispersion). The source of this anisotropy of the excitation spectrum is the anisotropy of the RKKY interaction in real space. It is worth mentioning that the standard slave-boson description used in a previous phenomenological model^{2,11} also predicts a highly anisotropic spectrum of HF excitations due to the sf -hybridization anisotropy in \mathbf{k} space.

If the levels $|\mp 5/2\rangle$ dominate in the ground state Kramers doublet $|G\pm\rangle$ (27) (see Sec. V B), then the effective intersite overlap integral \mathcal{T}_{ij}^{GG} is determined in this theory by the combination of hybridization matrix elements, $V_{\mathbf{k}\Lambda}^{i*} V_{\mathbf{k}\Lambda}^j / (\epsilon_F - E_f)$, which turns into zero for $\mathbf{k} = [1.0.0]$ (see, e.g., Ref. 24). This means that the f electron wave functions form the nonbonding states along this direction. Moreover, the expression $\overline{V}_{\mathbf{k}G}^{i*} V_{\mathbf{k}G}^j / (\epsilon_F - E_f)$ which determines in this case the mixing integrals \mathcal{B}_{ij}^{GE} turns into zero for $\mathbf{k} = [1.0.0]$ due to similar reasons. Thus one can expect that the main characteristic features of the interplay between the HF and CF states, including the pseudogap, would develop in the bc plane of the Brillouin zone. However, this kind of theory has an undesirable consequence: in the mean-field slave-boson approximation the spin and charge pseudogaps simply coincide, and this statement obviously contradicts the experimental data for CeNiSn.

Another version of the mean-field description of pseudogap in CeNiSn was presented recently in Ref. 25. It was postulated in this theory that the ground state of the Ce ion is the doublet $|\mp 3/2\rangle$, and the CF excitations were not taken into account. The pseudogap in the HF spectrum appeared due to the mentioned nonbonding character of the f - f overlap matrix element $\mathcal{T}^{GG}(\mathbf{k})$. Then the low-temperature behavior of the specific heat and magnetic susceptibility are determined by this pseudogap, and the satisfactory agreement between the theoretical description of these quantities and the experimental data for CeNiSn can be achieved.

As to the inelastic neutron scattering cross section, the theoretical results presented in Ref. 25 are too scanty to conclude about an agreement between the theory and the experiment. One can definitely mention the qualitative agreement, at least for the constant- E scans (Fig. 11 of Ref. 25 which is more or less similar to our Fig. 8). As to the constant- \mathbf{Q} scans, the slave-boson description is able to describe the pseudogap in the two-particle HF DOS (Fig. 10 of Ref. 25), although the experimental picture is, apparently, much more within reach than the smooth curves presented in that figure. One should mention also that the theoretical spectrum for $\mathbf{Q} = [1/2, 0, 0]$ presented in Fig. 10(b) demonstrates the peak in the a direction which must be weak in experiment because of the geometrical factor entering the neutron scattering cross section for this direction.^{7,9} It is unclear also whether this theory is able to describe the quasi-1D character of neutron scattering along the $[0, n + 1/2, Q_c]$ direction. On the face of it, this task seems to be rather difficult since the matrix element which governs the HF dispersion law behaves as $V^2(\hat{k}_x^2 + \hat{k}_y^2)(1 + 15\hat{k}_z^2)$ [see Eq. (2.10b) in Ref. 25]. Besides, the CF level scheme adopted in this model is not supported by the experimental data available.⁴ Finally, the coincidence of the charge and spin pseudogap in the mean-field slave-boson theory mentioned above does not allow one to reproduce the metallic character of low-temperature resistivity. The absence of T^2 in the theoretical curve $\rho(T)$ is clearly seen from Fig. 13 of Ref. 25.

The inelastic neutron scattering method is an adequate tool for observing the spin liquid excitations in the heavy-fermion materials. These measurements give the detailed information concerning the density of states of spinon particle-hole excitation spectrum, and the dispersion of various branches of spinon excitations can be restored by analyzing various constant- \mathbf{Q} and constant- E scans. The general picture of the low-energy excitation spectrum obtained from this analysis allowed us to describe also the low-temperature specific heat of CeNiSn (see also Ref. 26). All other important characteristics of this material, such as magnetic susceptibility, thermal expansion, NMR relaxation rate, etc., can also be described quantitatively within the same approach.

The specific features of the spin liquid excitation spectrum do not violate the conduction electron spectrum which remains essentially metallic, although the anisotropy of spin excitations can result in an anisotropy of scattering mechanism for conduction electrons, and the soft crystal-field excitations can influence their paramagnetic response. In any case, CeNiSn and related materials should be treated as metallic Kondo lattices with a specific type of spin excitation.

At the early stage of experimental investigations it was

assumed that CeNiSn belongs to the group of so-called Kondo insulators together with Ce₃Bi₄Pt₃ and related compounds.²⁸ The present study as well as recent experimental data^{5,6} show that the unusual behavior of orthorhombic compounds CeNiSn and CeRhSb is determined by the anomalous properties of spin excitation spectrum, whereas the real charge gap exists in Ce₃Bi₄Pt₃. It is worth mentioning that the spin gaplike effects were observed also in another orthorhombic material CeNi (Ref. 29) which is known to be a good metal. CeNi probably belongs to the same class of Kondo lattices with the heavy-fermion spectrum strongly perturbed by the interplay with the CF excitations.

ACKNOWLEDGMENTS

We are indebted to H. Kadowaki, S. Kambe, and T. Sato for timely providing us with experimental information and important comments, to N. V. Prokof'ev for valuable critical remarks, and to A. Yu. Yaresko for assistance in numerical computations. The support of Grant Nos. NWO 5-16501, INTAS 93-2834, and RFBR-95-02-04250 is acknowledged.

APPENDIX

To calculate the anisotropy factor in the Cornut-Coqblin Hamiltonian, one should expand the Bloch waves entering the RKKY interaction (11) and (13) in partial waves entering the hybridization integrals in Eq. (5) and then superimpose the direction connecting two ions with the quantization axis by means of the matrices of finite rotations.

In the case of short enough interionic distances one can neglect the influence of the angular dependence of the partial waves on the values of radial overlap integrals. This approximation¹⁵ in the simplest case of the doublet formed by the $j=5/2$ states with the same j_z value, i.e., $|\Gamma\nu\rangle=|j\pm M\rangle$ results in the following equation for the factor of the anisotropy of an exchange interaction:

$$B_G(\theta)=[B_M(\theta)]^2, \quad (\text{A1})$$

$$B_M(\theta)=\sum_{l=0,2,4,6}(-1)^{l/2}(2l+1)Z_l^M P_l(\cos\theta),$$

$$Z_l^M=\xi_M^2 O(l, M+1/2)+\eta_M^2 O(l, M-1/2),$$

$$\xi_M=\sqrt{(7+2M)/14}, \quad \eta_M=\sqrt{(7-2M)/14},$$

$$O(l, j)=C_{30/0}^{30} C_{3j/10}^{3j}.$$

Here $C_{3M'l}^{3M'}$ are the Clebsch-Gordan coefficients. This equation can be found in Ref. 15 for the case of $\theta=0$. Since the CF wave functions transform in accordance with the spherical group the only source of anisotropy is the definite direction of quantization axis which lowers symmetry to the axial one. Therefore the interaction depends on the polar angle θ only.

More complicated is the anisotropy factor for a mixed representation of Eq. (27). In this case the wave functions transform according to the irreducible representation of the trigonal group with the third-order rotational axis parallel to the quantization axis. In this case the RKKY interaction becomes ϕ dependent,

$$B_G(\theta, \phi)=\left\{1+\frac{2}{7}(5-9a^2)P_2(\cos\theta)+\frac{3}{7}(1+a^2)P_4(\cos\theta)-\frac{a\sqrt{1-a^2}}{7\sqrt{10}}P_4^3(\cos\theta)\cos(3\phi)\right\}^2. \quad (\text{A2})$$

For the specific cases of interaction ‘‘in plane’’ ($\theta=\pi/2$) and along the quantization axis ($\theta=0$) the factor B does not depend on the angle ϕ . Therefore the ratio between the ‘‘in plane’’ interaction and interaction along the z axis can be expressed in terms of a single parameter a entering the wave function (27),

$$\frac{B_G(\theta=\pi/2)}{B_G(\theta=0)}=\left\{\frac{1}{40}\frac{25+81a^2}{4-3a^2}\right\}^2. \quad (\text{A3})$$

It is seen from Eq. (A3) that $B_G(\theta=\pi/2)/B_G(\theta=0)\gg 1$ only when the $|1/2\rangle$ component of the crystal-field wave function (27) is dominant.

In the case of the large interionic distances the asymptotic behavior of the RKKY exchange integrals is dominated by $j_z=\pm 1/2$ partial waves,²⁷ and the ‘‘in plane’’ interaction is stronger than that along the quantization axis ($\theta=0$) in the case when the $|5/2\rangle$ component of the crystal-field wave function (27) is dominant.

¹P. Fulde, *Electron Correlations in Molecules and Solids*, 3rd ed. (Springer, Berlin, 1995), Chap. 13.

²Yu. Kagan, K.A. Kikoin, and N.V. Prokof'ev, *JETP Lett.* **57**, 600 (1993).

³T. Takabatake and H. Fujii, *Jpn. J. Appl. Phys. Ser. 8*, 254 (1993).

⁴P.A. Alekseev, V.N. Lazukov, E.S. Clementyev, E.V. Nefedova, I.P. Sadikov, M.N. Chlopkin, A.Yu. Muzhicka, I.L. Sashin, N.N. Efremova, and V. Bührer, *Sov. Phys. JETP* **79**, 665 (1994).

⁵T. Takabatake, G. Nakamoto, T. Yoshino, H. Fujii, K. Izawa, S. Nishigori, H. Goshima, T. Suzuki, T. Fujita, K. Maezawa, T. Hiraoka, Y. Okayama, I. Oguro, A.A. Menovsky, K. Neumaier, A. Brückl, and K. Andres, *Physica B* **223&224**, 413 (1996).

⁶K. Nakamura, Y. Kitaoka, K. Asayama, T. Takabatake, G. Nakamoto, H. Tanaka, and H. Fujii, *Physica B* **206&207**, 829 (1995).

⁷T.E. Mason, G. Aeppli, A.P. Ramirez, K.N. Clausen, C. Broholm, C.N. Stücheli, E. Bucher, and T.M.M. Palstra, *Phys. Rev. Lett.* **69**, 490 (1992).

⁸H. Kadowaki, T. Sato, H. Yoshizawa, T. Ekino, T. Takabatake, H. Fujii, L.P. Regnault, and Y. Ishikawa, *J. Phys. Soc. Jpn.* **63**, 2074 (1994).

⁹T. Sato, H. Kadowaki, H. Yoshizawa, T. Ekino, T. Takabatake, H. Fujii, L.P. Regnault, and Y. Ishikawa, *J. Phys. Condens. Matter* **7**, 8009 (1995).

¹⁰S. Kambe, S. Raymond, H. Suderow, J. McDonough, B. Fak, L.P. Regnault, and J. Flouquet, *Physica B* **223&224**, 135 (1996).

- ¹¹K.A. Kikoin, A. de Visser, K. Bakker, and T. Takabatake, *Z. Phys. B* **94**, 79 (1994).
- ¹²G. Baskaran, Z. Zou, and P.W. Anderson, *Solid State Commun.* **63**, 973 (1987).
- ¹³P. Coleman and N. Andrei, *J. Phys. Condens. Matter* **1**, 4057 (1989).
- ¹⁴K.A. Kikoin, M.N. Kiselev, and A.S. Mishchenko, *JETP Lett.* **60**, 600 (1994); *Physica B* **206&207**, 129 (1995).
- ¹⁵B. Coqblin and J.R. Schrieffer, *Phys. Rev.* **185**, 847 (1969).
- ¹⁶B. Cornut and B. Coqblin, *Phys. Rev. B* **5**, 4541 (1972).
- ¹⁷Yu. Kagan, K.A. Kikoin, and N.V. Prokof'ev, *Physica B* **182**, 201 (1992).
- ¹⁸I. Higashi, I.K. Kobayashi, T. Takabatake, and M. Kasaya, *J. Alloys Comp.* **193**, 300 (1993).
- ¹⁹S. Doniach, *Proc. Phys. Soc.* **91**, 86 (1967).
- ²⁰S. Nohara, H. Namatame, F. Fujimori, and T. Takabatake, *Phys. Rev. B* **47**, 1754 (1993).
- ²¹A.J. Nolten, M.Sci. thesis, Amsterdam University, Amsterdam, 1994.
- ²²A.J. Nolten, A. de Visser, F.E. Kayzel, J.J.M. Franse, H. Tanaka, and T. Takabatake, *Physica B* **206&207**, 825 (1995).
- ²³K.A. Kikoin, *J. Phys. Condens. Matter* **8**, 3601 (1996).
- ²⁴K. Hanzawa, K. Yamada, and K. Yosida, *J. Phys. Soc. Jpn.* **56**, 678 (1987).
- ²⁵H. Ikeda and K. Miyake, *J. Phys. Soc. Jpn.* **65**, 1769 (1996).
- ²⁶K.A. Kikoin, M.N. Kiselev, and A.S. Mishchenko, *Czech. J. Phys.* **46**, 1899 (1996).
- ²⁷B.R. Cooper, R. Siemann, D. Yang, P. Thayamballi, and A. Banerjee, in *The Handbook on the Physics and Chemistry of Actinides*, edited by A.J. Freeman and G.H. Lander (North-Holland, Amsterdam, 1985), Vol. 2, Chap. 6, pp. 435–500.
- ²⁸G. Aeppli and Z. Fisk, *Comm. Condens. Matter Phys.* **16**, 155 (1992).
- ²⁹V.N. Lazukov, P.A. Alekseev, E.S. Clementyev, R. Osborn, B. Rainford, I.P. Sadikov, O.D. Chistyakov, and N.B. Kolchugina, *Europhys. Lett.* **33**, 141 (1996).